

CLIMATE SCIENCE

State dependence of CO₂ forcing and its implications for climate sensitivity

Haozhe He^{1*†}, Ryan J. Kramer^{2,3†}, Brian J. Soden¹, Nadir Jeevanjee⁴

When evaluating the effect of carbon dioxide (CO₂) changes on Earth's climate, it is widely assumed that instantaneous radiative forcing from a doubling of a given CO₂ concentration (IRF_{2×CO₂}) is constant and that variances in climate sensitivity arise from differences in radiative feedbacks or dependence of these feedbacks on the climatological base state. Here, we show that the IRF_{2×CO₂} is not constant, but rather depends on the climatological base state, increasing by about 25% for every doubling of CO₂, and has increased by about 10% since the preindustrial era primarily due to the cooling within the upper stratosphere, implying a proportionate increase in climate sensitivity. This base-state dependence also explains about half of the intermodel spread in IRF_{2×CO₂}, a problem that has persisted among climate models for nearly three decades.

Radiative forcing (RF) refers to a change in net radiative flux at the top-of-atmosphere (TOA) due to an externally imposed perturbation in the Earth's energy balance (1, 2), such as anthropogenic activities (e.g., emission of greenhouse gases and aerosols) or natural events (e.g., volcanic eruptions). The Earth subsequently warms or cools to counteract the flux perturbation and restore radiative equilibrium. The RF is commonly separated into two parts (1, 3–6): (i) instantaneous radiative forcing (IRF), which measures the change in net radiative flux that results only from the change in forcing agents, and (ii) rapid adjustments, which consist of radiative perturbations induced by atmospheric responses to the IRF independent of any change in surface temperature. This study focuses on the IRF, which is considered to be the best-understood aspect of RF (7). For CO₂ perturbations, the IRF is responsible for approximately two-thirds of the total RF and is the fundamental driver of the rapid adjustments (1, 3–6, 8–12), wherein stratospheric cooling is the dominant adjustment to CO₂ forcing (11, 12). However, several previous studies have shown that the IRF from a doubling of CO₂ concentration (IRF_{2×CO₂}) varies by ~50% among climate models (10, 13–15). Although this spread has persisted for nearly three decades, its underlying cause has never been fully resolved.

Climate sensitivity is formally defined as the change in the global mean surface temperature required to restore radiative equilibrium in response to a doubling of CO₂ concentration ($\Delta T_{2\times\text{CO}_2}$). It is the most widely used met-

ric to quantify the susceptibility of the climate to an externally forced change, i.e., $\Delta T_{2\times\text{CO}_2} = -\text{RF}_{2\times\text{CO}_2}/\lambda$, where the radiative damping (λ , which is expressed in watts per meter squared per degree kelvin) is the efficiency at which radiative equilibrium is restored per unit change in surface temperature. The radiative damping depends on a number of well- and not-so-well-understood feedbacks within the climate system and is widely recognized to vary between climate models and in time as the climatological base state evolves. However, the intermodel variance in the RF_{2×CO₂} and its dependence on the base state are less well recognized. In this study, we demonstrate that the IRF_{2×CO₂} is not a constant, but rather depends on the climatological base state, as suggested by a recent analytical model (16). This state dependence not only explains about half of the intermodel variance in IRF_{2×CO₂}, but it also fundamentally reshapes our understanding of climate sensitivity, with important implications for both past and future climate changes.

Results

The Coupled Model Intercomparison Projects (CMIP) provide a series of coordinated experiments performed in support of the Intergovernmental Panel on Climate Change (IPCC) assessments in which model simulations are achieved using identical emission scenarios (17, 18). However, because determining the IRF requires additional calculations, it is not routinely computed for most experiments. In the first comprehensive RF comparison among climate models, Cess *et al.* (13) found that the IRF_{2×CO₂} ranged from ~3.3 to 4.7 W m⁻². Subsequent studies with newer generations of models found a similar range (10, 14). This spread was thought to mainly arise from intermodel differences in the parameterization of infrared absorption by CO₂ (15).

Double-call radiative transfer calculations are the most direct method for diagnosing the IRF in model simulations. To produce these

specialized online diagnostics, a second call is made to the radiation scheme at each time step. Radiative fluxes are recalculated with a hypothetical forcing agent perturbation, such as CO₂ at some increased concentration. These perturbations are solely used to diagnose the IRF and do not interact with the model simulation. Although only a few online double-call calculations were performed by climate models from CMIP5/6, the available output is particularly useful for investigating the state dependence of CO₂ IRF. To avoid the complicating effects of clouds in masking the IRF (7, 19, 20), we further simplified our analysis by limiting it to infrared CO₂ forcing at the TOA under clear-sky conditions.

Figure 1A shows the online double-call calculations available from the CMIP5/6 models for the Atmospheric Model Intercomparison Project (AMIP) historical experiment (amip), which contains the most online double-call calculations of any of the CMIP experiments (12 of 80 participating models provided calculations for this experiment; tables S1 and S2). The amip experiment consists of atmosphere-only model simulations that all used identical, time-varying sea surface temperatures observed over the period 1979 to 2008 as boundary conditions. The online double calls provided are for 4×CO₂; note that $\text{IRF}_{4\times\text{CO}_2} \approx 2 \times \text{IRF}_{2\times\text{CO}_2}$ for a given climate state (see the materials and methods). The results exhibit a large intermodel spread (ranging from ~4 to 8 W m⁻²), consistent with that observed in previous model generations (15).

To investigate the extent to which differences in the thermal structure of the climatological base state can explain the intermodel spread of IRF, we performed offline double-call IRF_{4×CO₂} calculations using original atmospheric profiles from the AMIP models and a single radiative transfer model (SOCRATES; see the materials and methods). In contrast to the online counterparts, the same radiative transfer parameterization is used in all of the offline calculations, so their intermodel spread is only due to differences in the climatological base states. The strong correlation ($r = 0.82$) between the IRFs from the online and offline double-call calculations (Fig. 1B) suggests that more than half of the intermodel variance in IRF_{4×CO₂} results from differences in climatological base states, not from differences in representing the spectral absorption of CO₂. This is consistent with a recent study by Pincus *et al.* (19), who computed IRF from different radiative transfer schemes but using the same climatological base state, finding a much smaller spread in IRF_{4×CO₂} than in the online double calls (Fig. 1A). Together, these studies provide compelling evidence to suggest that intermodel differences in the climatological base state are an essential contributor to the spread in CO₂ IRF.

The influence of the base state on CO₂ IRF is more clearly illustrated in the coupled model simulations from CMIP6, in which a 1% per year

¹Rosenstiel School of Marine, Atmospheric and Earth Science, University of Miami, Miami, FL, USA. ²Goddard Earth Science Technology and Research II, University of Maryland at Baltimore County, Baltimore, MD, USA. ³Climate and Radiation Laboratory, NASA Goddard Space Flight Center, Greenbelt, MD, USA.

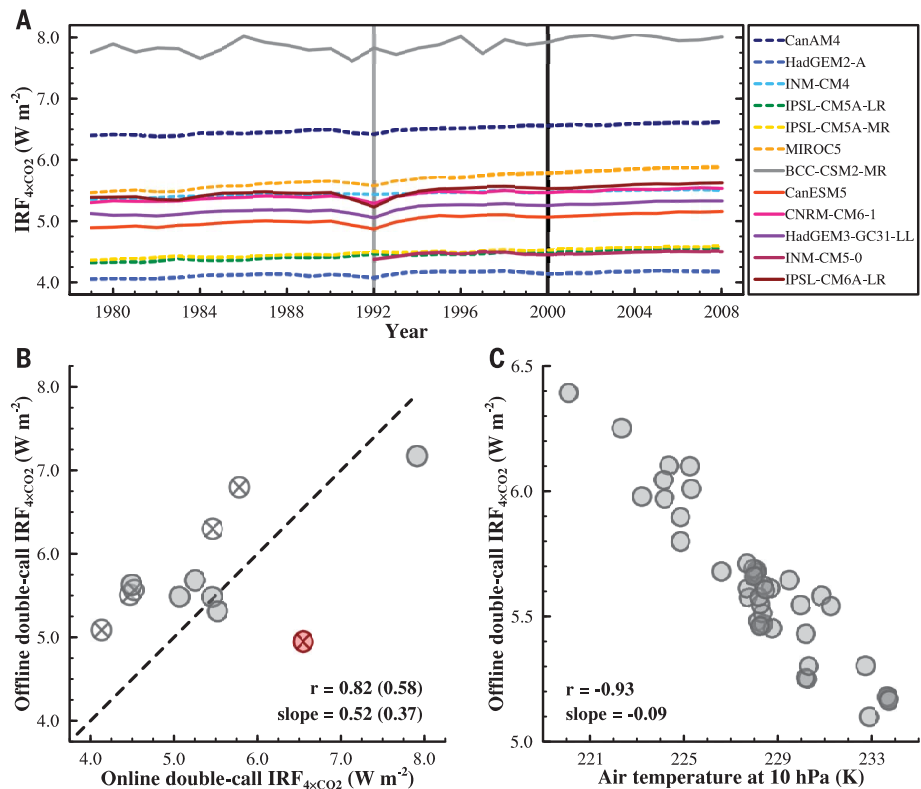
⁴Geophysical Fluid Dynamics Laboratory, Princeton, NJ, USA.

*Corresponding author. Email: haozhe.he@miami.edu

†Present address: High Meadows Environmental Institute, Princeton University, Princeton, NJ, USA.

‡Present address: Geophysical Fluid Dynamics Laboratory, Princeton, NJ, USA.

Fig. 1. Intermodel spread in $\text{IRF}_{4\times\text{CO}_2}$ and its causes. (A) Time series of all available online double-call $\text{IRF}_{4\times\text{CO}_2}$ with base state from amip experiments for CMIP5/6 models. The black vertical reference line highlights the $\text{IRF}_{4\times\text{CO}_2}$ values used in (B), and the gray line accentuates the brief declines in the magnitude of the $\text{IRF}_{4\times\text{CO}_2}$ in the year 1992, after the eruption of Mount Pinatubo. (B) Comparison of the $\text{IRF}_{4\times\text{CO}_2}$ in the year 2000 from the online and offline double-call calculations. The gray filled circles represent models from CMIP6, and the open circles with a cross inside show models from CMIP5. The red filled circle with a cross inside highlights the outlier model (i.e., CanAM4). Because the vertical IRF profile of CanAM4 shows an increase with height within the stratosphere [see figure 3 of Chung and Soden (10)], it differs from the common expectation based on the negative lapse rate within the stratosphere. It is reasonable to exclude the results of the CanAM4 from the spread contribution analysis. The values in front of (in) parentheses shown in (B) are values calculated without (with) the outlier model CanAM4. (C) A scatterplot of global and annual mean air temperature at 10 hPa of each model in the year 2000 of the amip experiment versus its corresponding offline double-call $\text{IRF}_{4\times\text{CO}_2}$.



increase is imposed on the atmospheric CO_2 concentration (1pctCO₂; Fig. 2). Although only two models (Fig. 2A, solid lines) submitted online double-call calculations, the results reveal a substantial growth in $\text{IRF}_{4\times\text{CO}_2}$ as the climatological base state evolves. For both models, $\text{IRF}_{4\times\text{CO}_2}$ increases from $\sim 5 \text{ W m}^{-2}$ when $\text{IRF}_{4\times\text{CO}_2}$ is computed in a preindustrial climate to $\sim 8 \text{ W m}^{-2}$ when it is computed in an elevated- CO_2 climate. This challenges the widely held assumption that the $\text{IRF}_{2\times\text{CO}_2}$ is constant (21–23); on the contrary, it demonstrates that the CO_2 IRF is a dynamic quantity that changes substantially as the climate changes.

To verify this result, we performed a series of line-by-line and SOCRATES offline double-call calculations using the full suite of CMIP5/6 coupled simulations under the 1pctCO₂ scenario (Fig. 2A, markers). These results both confirm the marked increase in $\text{IRF}_{4\times\text{CO}_2}$ using a much larger ensemble of models and, because the same radiative transfer scheme is used for all offline calculations, indicate that changes in the climatological base state are responsible for this increase. Note that the climatological base state here includes the thermal structure as well as the base-state CO_2 concentration (24–26), both of which vary with each time step. However, most of the $\text{IRF}_{4\times\text{CO}_2}$ increases are due to the evolution of thermal structure, especially for the first doubling of base-state CO_2 concentration (fig. S1).

According to the analytical model of Jeevanjee *et al.* (16), the dependence of CO_2

IRF on the climatological base state can be understood in terms of dependence on the emission temperature of both stratosphere and troposphere as follows:

$$\mathcal{F} = 2l \ln \left(\frac{q_f}{q_i} \right) [\pi B(v_0, \bar{T}_{\text{em}}) - \pi B(v_0, \bar{T}_{\text{strat}})]$$

Where l is the “spectroscopic decay” parameter of 10.2 cm^{-1} , q_i is the initial CO_2 concentration, q_f is the final CO_2 concentration, and $\pi B(v_0, \bar{T}_{\text{em}})$ and $\pi B(v_0, \bar{T}_{\text{strat}})$ are the hemispherically integrated Planck function at peak absorption wave number of CO_2 with the tropospheric and the stratospheric emission temperature, respectively (see the materials and methods). The latter refers to the temperature of the upper stratosphere, where unit optical depth is achieved by the peak of the CO_2 absorption band, whereas the former depends on surface temperature and free troposphere relative humidity. This model has been used to help explain the spatially inhomogeneous distribution of IRF that results from a spatially uniform increase of CO_2 (27).

As CO_2 increases in the 1pctCO₂ simulations, the surface temperature warms and the stratosphere cools roughly linearly over time (Fig. 2, B and C). To assess the relative contributions of these changes in climate to the increase in $\text{IRF}_{4\times\text{CO}_2}$, we include results from the CMIP6 abrupt-4 $\times\text{CO}_2$ experiment (Fig. 2, dashed lines; only one model provided online double-call calculations for this experiment). In contrast

to the 1pctCO₂ experiment, CO_2 is instantly quadrupled in the abrupt-4 $\times\text{CO}_2$ experiment, causing the surface to warm rapidly over the first few decades before leveling off. The stratosphere adjusts even more rapidly, equilibrating to a new temperature within the first year.

The contrasting temporal evolution of the climate between these two scenarios is reflected in the $\text{IRF}_{4\times\text{CO}_2}$. For instance, the $\text{IRF}_{4\times\text{CO}_2}$ with abrupt-4 $\times\text{CO}_2$ base-state exhibits only a mild increase with global mean surface warming (Fig. 2), indicating a relatively weak dependence of the CO_2 IRF on surface temperature. By contrast, $\text{IRF}_{4\times\text{CO}_2}$ in the 1pctCO₂ experiment exhibits a much larger increase over time despite having a similar change in global mean surface temperature. Physically, the CO_2 IRF represents a swap of tropospheric emission for stratospheric emission (16), and because the temperature change within the stratosphere is much larger than that at the surface and within the troposphere, the IRF increase closely follows the stratosphere cooling, suggesting a dominant role of stratospheric temperature on the CO_2 IRF. We emphasize that the results shown in Fig. 2A represent IRF only and do not include the stratospheric adjustment. Rather, the changes in IRF over time reflect the impact of the stratospheric adjustment from prior CO_2 changes on the base state, which in turn amplifies the IRF that would result from a subsequent “hypothetical” quadrupling of CO_2 . Because cloud masking has virtually no influence on stratospheric emission,

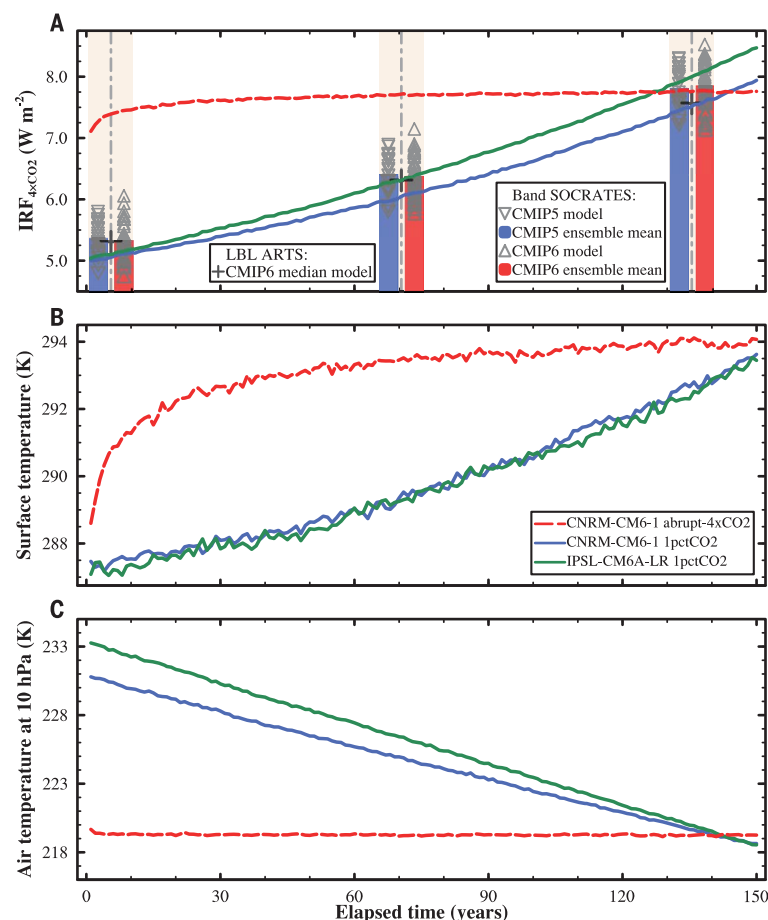


Fig. 2. CO₂ IRF increases as the surface warms and the stratosphere cools. (A to C) Time series of global and annual mean online double-call IRF_{4xCO2} (A), surface temperature (B), and air temperature at 10 hPa (C) from models CNRM-CM6-1 and IPSL-CM6A-LR. Three highlighted time slices in (A) are years 1 to 10, 66 to 75, and 131 to 140. Overlaid gray triangles represent the global and time mean SOCRATES offline double-call IRF_{4xCO2} with corresponding atmospheric profiles of 1pctCO₂ simulations from CMIP5/6 models. The black plus symbols show the global mean ARTS offline double-call IRF_{4xCO2} with time mean atmospheric profiles from the CMIP6 model, which has the median SOCRATES double-call IRF_{4xCO2} value. Similar results from another line-by-line model (PyRADs) are shown in fig. S1. Note that the results in (A) represent IRF only and do not include any rapid adjustment. Rather, the changes in IRF over time reflect the impact of the effects from prior CO₂ changes on the base state, which in turn amplifies the IRF that would result from a subsequent “hypothetical” quadrupling of CO₂.

the dominant role of stratospheric temperature also remains under all-sky conditions.

The state dependence of CO₂ IRF on the surface temperature and stratospheric temperature is also evident in the amip simulations (Fig. 1A). Because these simulations adopt the same sea surface temperature as their boundary conditions, our results imply that differences in stratospheric temperature are primarily responsible for the intermodel spread in IRF_{4xCO2}. To confirm the role of the stratospheric temperature on the IRF spread, we also performed the SOCRATES offline double-call IRF calculations using the same amip base states and determined its correlation with the corresponding air temperature at 10 hPa, which is the highest level of CMIP5 standard pressure-level outputs [and is closest to the

level with unit optical depth achieved by the peak of the CO₂ absorption band (16, 20, 28)]. A high, significant correlation was found between the IRF and stratospheric temperature across both the CMIP6 and CMIP5 models (Fig. 1C and fig. S2), highlighting that biases in stratospheric temperature play a dominant role in causing the intermodel spread in CO₂ IRF.

The overwhelming effect of stratospheric temperature over surface temperature is also reflected in the brief declines for many models in the magnitude of the IRF_{4xCO2} in the year 1992, after the eruption of Mount Pinatubo (Fig. 1A). On average and across the models, there was only a 0.2 K surface temperature decrease but an ~1 K temperature increase at 10 hPa in 1992 compared with 1991.

The analytical model of CO₂ IRF by Jeevanjee *et al.* (16) replicates the offline double-call IRF_{4xCO2} of CMIP6 and CMIP5 with high correlations for abrupt-4xCO₂ simulations (Fig. 3A and fig. S3), providing a computationally efficient alternative for investigating the sensitivity of the CO₂ IRF to stratospheric temperatures. Because the 10 hPa temperatures cool at a similar rate for all models under 1pctCO₂ scenarios from CMIP6 and CMIP5 (Fig. 3B and fig. S4), the temperatures at this level have nearly identical intermodel spread at the beginning and end of the simulations. This suggests that intermodel spread in the CO₂ IRF arises explicitly from differences in the initial stratospheric temperatures under preindustrial conditions. We confirmed this with the analytical model, finding that it produces the same IRF intermodel spread and is highly correlated with the offline double-call calculations even when the initial, preindustrial upper stratospheric temperatures are used as input for every time step instead of the actual, time-varying temperature from the corresponding abrupt-4xCO₂ simulations (Fig. 3C and fig. S5).

Our results demonstrate that CO₂ IRF increases as the climate changes in response to increased CO₂. Online and offline double-call calculations from the CMIP6 historical simulations (Fig. 4A, fig. S6A, and table S3) indicate that IRF_{4xCO2} is ~10% larger today than it was in the mid-19th century due to the change in base state, which was primarily from stratospheric cooling. This amplification arises predominantly from the increase in well-mixed greenhouse gases over this period (Fig. 4A). Thus, the IRF_{4xCO2} increases over time because the CO₂-induced cooling of the stratosphere makes any subsequent change in CO₂ more potent.

Because it is the sum of the IRF and rapid adjustments, known as the total or “effective” RF, that ultimately drives climate change (1, 3, 4, 29), it is important to understand the extent to which the rapid adjustments may also depend on the base state. To investigate the state dependence of the adjustments, we used atmosphere-only model simulations forced by boundary conditions of both the preindustrial era (piClim-control) and recent decades (amip), along with their corresponding 4xCO₂ counterparts (piClim-4xCO₂ and amip-4xCO₂; see the materials and methods and table S4). The amip simulation not only has a higher prescribed CO₂ concentration than that of the piClim-control simulation, but also has a cooler stratosphere temperature, allowing us to quantify the magnitude of the adjustments under two different base states.

The stratospheric adjustment is the most important of the rapid adjustments to CO₂ forcing, typically an order of magnitude larger than tropospheric adjustments (11, 12). The sum

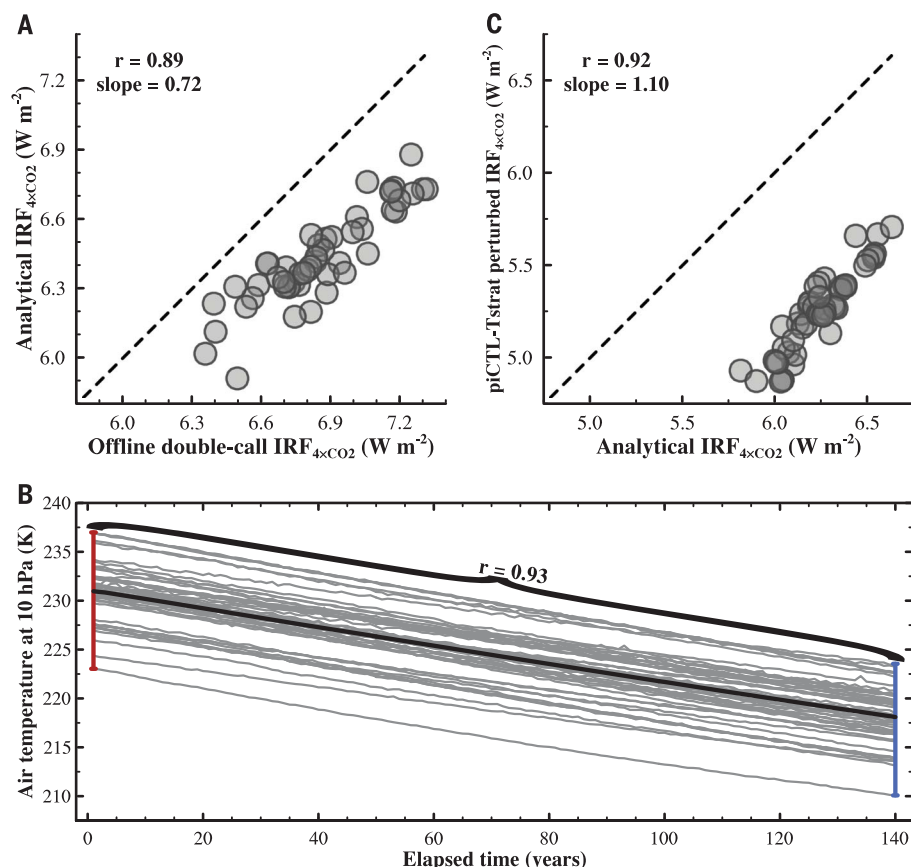


Fig. 3. Differences in initial stratospheric temperatures across models explain approximately half of the intermodel spread in $IRF_{4\times CO_2}$, as shown using abrupt- $4\times CO_2$ experiments. (A) Comparison of global and time mean $IRF_{4\times CO_2}$ in years 121 to 140 from the offline double-call and analytical model calculations with base state from abrupt- $4\times CO_2$ experiments. The correlation between global and time mean $IRF_{4\times CO_2}$ in every 10 of 150-year experiments from the offline double-call and the analytical model calculations ranges from 0.88 to 0.89. (B) Time series of global and annual mean 10 hPa air temperature under 1pctCO2 scenario from CMIP6 models. Each gray line in (B) represents the 10 hPa temperature evolution of a model, and the thick black line shows the multimodel ensemble mean. The curly bracket in (B) highlights the correlation between 10 hPa air temperature at years 1 and 140. (C) Comparison of the global and time mean original analytical $IRF_{4\times CO_2}$ in years 2 to 11 with that obtained with perturbed stratospheric emission temperature from piControl runs (piCTL-Tstrat). The correlation between the global and time mean $IRF_{4\times CO_2}$ from the original and piCTL-Tstrat perturbed calculations ranges from 0.90 to 0.92.

of IRF and stratospheric adjustment, or the “stratospheric adjusted” RF, are roughly equal at the tropopause and the TOA (30), thus providing an accurate and computationally efficient analog for the total RF. Figure S6 compares the IRF, stratospheric adjustments, and stratospheric adjusted RF from the CO_2 quadrupling for the two different base states (see the materials and methods). The amip simulations exhibit a larger IRF (fig. S6A; 0.38 W m^{-2}) compared with that obtained under preindustrial conditions because of the cooler stratosphere. There is a nearly identical difference in the stratospheric adjusted RF between the two sets of experiments (fig. S6C; 0.34 W m^{-2}) because almost no difference is seen in the stratospheric adjustments (fig. S6B; -0.03 W m^{-2}). Note that the abovementioned ensemble mean

forcing differences are also corroborated by differences shown for individual models. Even though the direct contribution of the base state to the intermodel spread in stratospheric adjusted RF and total RF is smaller than it is for the IRF, because additional sources of spread contribute, there are high, significant correlations between the IRF and both the stratospheric-adjusted RF and total RF (fig. S7, A and B).

The state dependence of both the IRF and stratospheric adjustment was further explored using the more realistic, online, interactive, coupled simulations forced by abruptly halving, doubling, and quadrupling CO_2 concentration of the preindustrial era (abrupt- $0.5\times CO_2$, abrupt- $2\times CO_2$, and abrupt- $4\times CO_2$, respectively; see the materials and methods and table S5).

As expected, for every model analyzed, we found that the IRF grew in magnitude across the three sets of experiments for each successive CO_2 doubling (fig. S8). The stratospheric-adjusted RF exhibited a nearly identical increase across the experiments, with the stratospheric adjustment only weakly offsetting the increases. Similar increases per CO_2 doubling have also been found for the total RF estimated from atmosphere-only simulations with fixed sea surface temperatures (31). This indicates that with almost no counteracting effects from rapid adjustments, the radiative effects from the stratospheric temperature base-state dependence of the IRF extend to the total RF (figs. S6 to S8) and thus on to climate sensitivity.

Changes in climate sensitivity can therefore arise from both changes in climate feedback and changes in IRF. More generally, these results indicate that despite the logarithmic dependence of CO_2 absorption (28), the climate becomes increasingly sensitive to a doubling of CO_2 as the base-state CO_2 concentration increases and the stratosphere cools correspondingly. The $IRF_{2\times CO_2}$ increases by $\sim 25\%$ for each doubling of base-state CO_2 concentration (i.e., the $IRF_{2\times CO_2}$ increases by 24 and 29% for the first and second doubling of base-state CO_2 concentration, respectively; Fig. 2A). Because the IRF accounts for about two-thirds of the total RF from CO_2 (1, 10–12), this implies that $\Delta T_{2\times CO_2}$ increases by ~ 15 to 20% for each doubling of CO_2 just from changes in the IRF. This state dependence of the $IRF_{2\times CO_2}$, and thus $\Delta T_{2\times CO_2}$, has not been accounted for in the latest IPCC reports.

Potential climate implications

Because the upper stratospheric temperature plays a dominant role in determining the magnitude of the CO_2 IRF, any changes in atmospheric composition that perturb stratospheric temperature could subsequently affect the climate. Consider the recent example of polar ozone depletion (32–34), which strongly influences the temperature structure within the stratosphere (35). The ozone depletion since the 1970s has led to strong cooling within the stratosphere. By cooling the stratosphere, ozone depletion makes the forcing from the increase in CO_2 over this period more potent. Although the stratospheric ozone loss mainly occurs in the lower stratosphere (36, 37), the associated cooling also contributes to a decline in infrared emission from the lower to the upper stratosphere, thus strengthening the CO_2 IRF at the TOA.

Here, we examined this nonlinear interaction between ozone depletion-induced cooling and CO_2 IRF by comparing a 10-member ensemble of model simulations that use all historical forcings with the corresponding sum of model simulations in which each historical

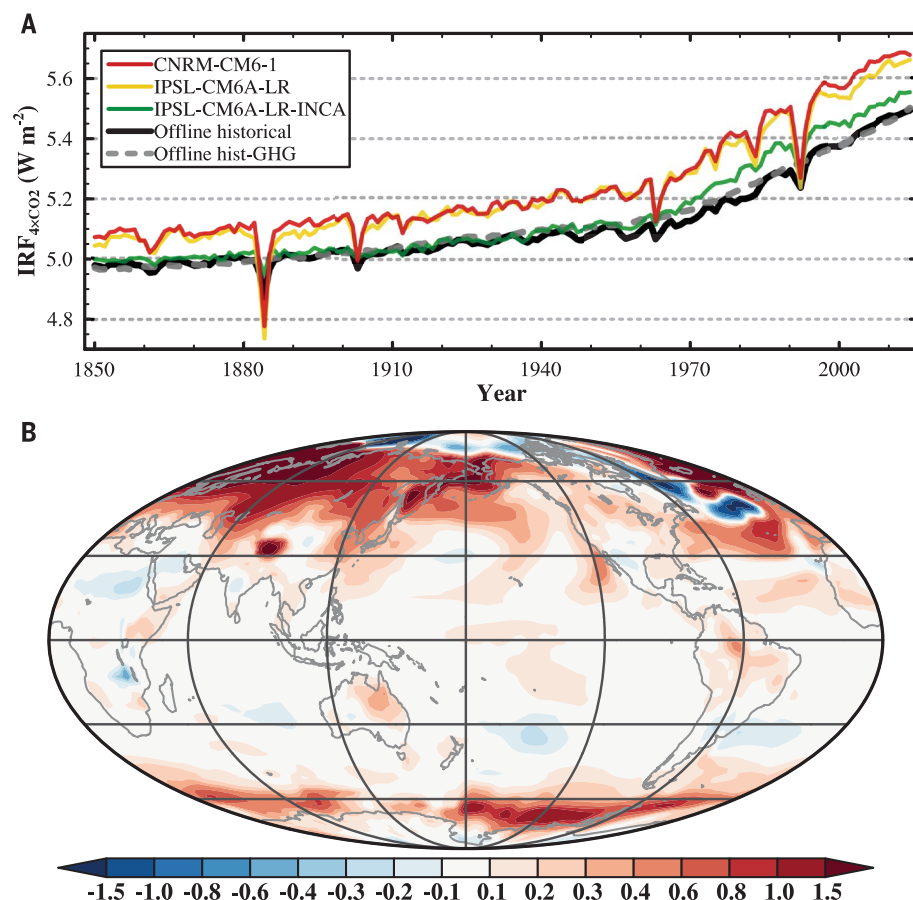


Fig. 4. Any forcing that perturbs the stratospheric temperature can further affect the climate by modulating the radiative forcing by CO₂. (A) Time series of three available online double-call IRF_{4xCO₂} from CMIP6 historical simulations and the multimodel ensemble mean of corresponding offline double-call IRF_{4xCO₂} for CMIP6 models with both historical and historical well-mixed greenhouse gas-only (hist-GHG) simulations. (B) Ensemble mean map of the indirect surface warming effect of ozone depletion during the period 1985 to 2014.

forcing is imposed independently (see the materials and methods). According to our theory, model simulations in which ozone loss and CO₂ increase coincide should have a larger CO₂ forcing (and thus greater surface warming) than the sum of individual model simulations, in which each forcing is imposed separately in isolation from the other. The CO₂ forcing in the latter is smaller because it is not enhanced by ozone depletion-induced cooling. We computed the indirect surface warming effect of ozone depletion by taking the ensemble mean difference in surface temperature anomalies between these two sets of experiments averaged over the period 1985 to 2014 (see the materials and methods).

As predicted, the sign and spatial distribution of the nonlinear contribution of ozone loss to CO₂ IRF is consistent with a base-state dependence of IRF (Fig. 4B). Most of the indirect surface warming effect occurs around the poles, where the local stratosphere has the strongest cooling, although some heat transport may also be playing a role (38, 39). The

smaller warming over the southern high latitudes likely reflects the greater rate of ocean heat uptake by the Southern Ocean (40, 41). This supports the premise that any forcing agent changes that perturb the stratospheric temperature could also affect the climate by modulating the CO₂ IRF at the TOA even without changing the CO₂ amount.

Our findings may also help us better understand past climate events such as the end-Devonian mass extinction and the Paleoproterozoic “snowball Earth” conditions, which occurred after similar but considerably stronger perturbations [i.e., a substantial drop in stratosphere ozone (42) and the inevitable development of an ozone layer (43, 44), respectively]. The base-state dependence of the CO₂ IRF may have implications for how other related metrics are defined, such as global warming potential and efficacy of non-CO₂ forcing (9, 29), because they are quantified relative to the radiative effects of a CO₂ perturbation. These metrics are often used in policy discussions, so it will be particularly important to determine whether

they must be redefined with consideration of the dynamic (i.e., nonconstant) behavior of CO₂ IRF.

Additionally, our results may have implications for geoengineering and climate change mitigation (45). Taking 1992, the year after the 1991 eruption of Mount Pinatubo, as an example, the injected volcanic aerosols within the stratosphere not only cooled the surface by reflecting more solar radiation back to the space, but they also warmed the stratosphere by increasing the atmospheric absorption of sunlight in the stratosphere (46, 47). The resulting stratospheric warming weakened the CO₂ IRF (Figs. 1A and 4A) and reduced the warming efficacy of CO₂. Because most geoengineering approaches involving stratospheric aerosol injection use reflective aerosols [e.g., sulfate (48)], alternative approaches that use more absorbing aerosols (e.g., black carbon) may warrant consideration, because this could effectively reduce the CO₂ greenhouse effect by warming the upper stratosphere (fig. S9) (49, 50).

Finally, we note that the model simulations of stratospheric temperature can be easily constrained with observations. Across multiple sets of observations and reanalyses (see the materials and methods and table S6), the global and annual mean 10 hPa air temperature had an uncertainty range of 226.6 to 228.4 K in the year 2020. This ~1.8 K difference in base state would translate to only an ~0.16 (0.18) W m⁻² IRF_{4xCO₂} uncertainty for CMIP6 (CMIP5) models (Fig. 1C and fig. S2). This highlights the importance of accurately representing the stratosphere when projecting future CO₂-induced climate change and the potential to better constrain model projections using observations, further emphasizing the importance of continuing observations in Earth’s middle and upper atmosphere (51).

REFERENCES AND NOTES

1. G. Myhre et al., in *Climate Change 2013 - The Physical Science Basis. Contribution of Working Group I to the Fifth Assessment Report of the Intergovernmental Panel on Climate Change* (Cambridge Univ. Press, 2009), pp. 659–740.
2. R. J. Kramer et al., *Geophys. Res. Lett.* **48**, e2020GL091585 (2021).
3. O. Boucher et al., in *Climate Change 2013 - The Physical Science Basis. Contribution of Working Group I to the Fifth Assessment Report of the Intergovernmental Panel on Climate Change* (Cambridge Univ. Press, 2009), pp. 571–657.
4. S. C. Sherwood et al., *Bull. Am. Meteorol. Soc.* **96**, 217–228 (2015).
5. P. M. Forster et al., *J. Geophys. Res. Atmos.* **121**, 12,460–12,475 (2016).
6. V. Ramaswamy et al., *Meteorol. Monogr.* **59**, 14.1–14.101 (2019).
7. M. G. Mlynarczyk et al., *Geophys. Res. Lett.* **43**, 5318–5325 (2016).
8. K. P. Shine, J. Cook, E. J. Highwood, M. M. Joshi, *Geophys. Res. Lett.* **30**, 2003GL018141 (2003).
9. J. Hansen et al., *J. Geophys. Res.* **110** (D18), D18104 (2005).
10. E.-S. Chung, B. J. Soden, *Environ. Res. Lett.* **10**, 074004 (2015).
11. C. J. Smith et al., *Geophys. Res. Lett.* **45**, 12023–12031 (2018).
12. C. J. Smith et al., *Atmos. Chem. Phys.* **20**, 9591–9618 (2020).
13. R. D. Cess et al., *Science* **262**, 1252–1255 (1993).
14. W. D. Collins et al., *J. Geophys. Res.* **111**, D14317 (2006).
15. B. J. Soden, W. D. Collins, D. R. Feldman, *Science* **361**, 326–327 (2018).

16. N. Jeevanjee, J. T. Seeley, D. Paynter, S. Fueglistaler, *J. Clim.* **34**, 9463–9480 (2021).
 17. K. E. Taylor, R. J. Stouffer, G. A. Meehl, *Bull. Am. Meteorol. Soc.* **93**, 485–498 (2012).
 18. V. Eyring *et al.*, *Geosci. Model Dev.* **9**, 1937–1958 (2016).
 19. R. Pincus *et al.*, *J. Geophys. Res. Atmos.* **125**, e2020JD033483 (2020).
 20. X. Huang *et al.*, *J. Geophys. Res. Atmos.* **127**, e2022JD037598 (2022).
 21. G. Myhre, E. Highwood, K. P. Shine, F. Stordal, *Geophys. Res. Lett.* **25**, 2715–2718 (1998).
 22. M. Etminan, G. Myhre, E. J. Highwood, K. P. Shine, *Geophys. Res. Lett.* **43**, 12,614–12,623 (2016).
 23. B. Byrne, C. Goldblatt, *Geophys. Res. Lett.* **41**, 152–160 (2014).
 24. R. Caballero, M. Huber, *Proc. Natl. Acad. Sci. U.S.A.* **110**, 14162–14167 (2013).
 25. W. Zhong, J. D. Haigh, *Weather* **68**, 100–105 (2013).
 26. J. T. Seeley, “Convection, radiation, and climate: Fundamental mechanisms and impacts of a changing atmosphere,” thesis, University of California, Berkeley (2018).
 27. Y. Huang, X. Tan, Y. Xia, *J. Geophys. Res. Atmos.* **121**, 2780–2789 (2016).
 28. D. M. Romps, J. T. Seeley, J. P. Edman, *J. Clim.* **35**, 4027–4047 (2022).
 29. K. P. Shine, R. G. Derwent, D. J. Wuebbles, J.-J. Morcrette, in *Climate Change: The IPCC Scientific Assessment* (Cambridge Univ. Press, 1990), pp. 41–68.
 30. K. P. Shine, G. Myhre, *J. Adv. Model. Earth Syst.* **12**, e2019MS001951 (2020).
 31. I. Mitevski, L. M. Polvani, C. Orbe, *Geophys. Res. Lett.* **49**, e2021GL097133 (2022).
 32. C. M. Bitz, L. M. Polvani, *Geophys. Res. Lett.* **39**, 2012GL053393 (2012).
 33. E. A. Barnes, N. W. Barnes, L. M. Polvani, *J. Clim.* **27**, 852–867 (2014).
 34. L. M. Polvani, M. Previdi, M. R. England, G. Chiodo, K. L. Smith, *Nat. Clim. Chang.* **10**, 130–133 (2020).
 35. K. P. Shine *et al.*, *Q. J. R. Meteorol. Soc.* **129**, 1565–1588 (2003).
 36. P. M. de Forster, K. P. Shine, *J. Geophys. Res. Atmos.* **102**, 10841–10855 (1997).
 37. A. C. Maycock *et al.*, *Geophys. Res. Lett.* **45**, 9919–9933 (2018).
 38. M. F. Stuecker *et al.*, *Nat. Clim. Chang.* **8**, 1076–1081 (2018).
 39. Q. Fu, S. Solomon, H. A. Pahlavan, P. Lin, *Environ. Res. Lett.* **14**, 114026 (2019).
 40. P. J. Durack, P. J. Gleckler, F. W. Landerer, K. E. Taylor, *Nat. Clim. Chang.* **4**, 999–1005 (2014).
 41. D. Roemmich *et al.*, *Nat. Clim. Chang.* **5**, 240–245 (2015).
 42. J. E. A. Marshall, J. Lakin, I. Troth, S. M. Wallace-Johnson, *Sci. Adv.* **6**, eaba0768 (2020).
 43. I. H. Campbell, C. M. Allen, *Nat. Geosci.* **1**, 554–558 (2008).
 44. M. R. Warke *et al.*, *Proc. Natl. Acad. Sci. U.S.A.* **117**, 13314–13320 (2020).
 45. J. G. Shepherd, *Geoengineering the climate: Science, governance, and uncertainty* (Royal Society, 2009).
 46. A. Robock, *Rev. Geophys.* **38**, 191–219 (2000).
 47. D. T. Shindell, G. A. Schmidt, M. E. Mann, G. Faluvegi, *J. Geophys. Res.* **109** (D5), 2003JD004151 (2004).
 48. P. J. Rasch *et al.*, *Philos. Trans. A Math. Phys. Eng. Sci.* **366**, 4007–4037 (2008).
 49. A. J. Ferraro, E. J. Highwood, A. J. Charlton-Perez, *Geophys. Res. Lett.* **38**, L24706 (2011).
 50. B. Kravitz, A. Robock, D. T. Shindell, M. A. Miller, *J. Geophys. Res.* **117**, 2011JD017341 (2012).
 51. M. G. Mlynarczyk, J. Yue, J. McCormack, R. S. Liebermann, N. J. Livesey, *Eos* **102**, (2021).
 52. Data and code for: H. He, R. J. Kramer, B. J. Soden, N. Jeevanjee, State dependence of CO₂ forcing and its implications for climate sensitivity, Zenodo (2023); <https://doi.org/10.5281/zenodo.10152455>.
- ACKNOWLEDGMENTS**
- We thank A. Sima, C. Smith, and P. Nabat for clarifying CMIP standard online double-call methods; J. Seeley for insightful discussions at the initial stage of this work; and D. Paynter and P. Lin for helpful comments. **Funding:** This work was supported by the National Oceanic and Atmospheric Administration (award NA18OAR4310269 to H.H., R.J.K., and B.J.S. and award NA21OAR4310351 to H.H. and B.J.S.) and the National Aeronautics and Space Administration (Science of Terra, Aqua and Suomi-NPP grant 80NSSC21K1968 to R.J.K.). **Author contributions:** Conceptualization: H.H., R.J.K., B.J.S., N.J.; Funding acquisition: R.J.K., B.J.S., N.J.; Investigation: H.H., R.J.K., B.J.S., N.J.; Methodology: H.H., R.J.K., B.J.S., N.J.; Project administration: B.J.S.; Supervision: B.J.S.; Visualization: H.H.; Writing – original draft: H.H., R.J.K., B.J.S.; Writing – review and editing: H.H., R.J.K., B.J.S., N.J. **Competing interests:** The authors declare no competing interests. **Data and materials availability:** The CMIP6 data are available at <https://esgf-node.llnl.gov/search/cmip6/>, and CMIP5 data are available at <https://esgf-node.llnl.gov/projects/cmip5/>. The CMIP6/5 models used in this work are listed in tables S1 to S5 in the supplementary materials. The AIRS temperature observations, Aura MLS retrievals, Aqua IR-only, SNPP, and NOAA-20 products produced using the CLIMCAPS algorithm and the MERRA-2 reanalysis data are available at <https://disc.gsfc.nasa.gov/datasets/>. The processed level 2A SABER products are available at https://data.gats-inc.com/saber/custom/Temp_O3_H2O/v2.0/. The ERA5 reanalysis data are available at <https://cds.climate.copernicus.eu/cdsapp#!/dataset/reanalysis-era5-pressure-levels-monthly-means?tab=overview>. The NCEP-DOE Reanalysis 2 data are available at <https://psl.noaa.gov/data/gridded/data.ncep.reanalysis2.pressure.html>. The benchmark radiative forcing values are available at <https://github.com/RobertPincus/rfmp-benchmark-paper-figures>. SOCRATES is available from <https://code.metoffice.gov.uk/trac/socrates> but requires a free account from the UK Met Office to access the website. ARTS is available at <https://www.radiativetransfer.org/getarts/>. PyRADs is available at <https://github.com/danielkoll/PyRADs>. The data and scripts used to produce the figures and the code to reproduce the data for this paper are available at Zenodo (52). **License information:** Copyright © 2023 the authors, some rights reserved; exclusive licensee American Association for the Advancement of Science. No claim to original US government works. <https://www.science.org/about/science-licenses-journal-article-reuse>
- SUPPLEMENTARY MATERIALS**
- science.org/doi/10.1126/science.abq6872
Materials and Methods
Figs. S1 to S9
Tables S1 to S6
References (53–76)
- Submitted 25 April 2022; accepted 30 October 2023
10.1126/science.abq6872